


Control of fatigue failure mechanisms in multilayer coatings by varying the architectural parameters of an intermetallic interlayer

Songsong Lu^{1,2}  | Richard Cook³ | Yi Zhang⁴ | Philippa Reed¹

¹Mechanical Engineering Group, Faculty of Engineering and Physical Sciences, University of Southampton, Southampton, UK

²Institute of Solid Mechanics, School of Aeronautic Science and Engineering, Beihang University (BUAA), Beijing, China

³nCATS, Faculty of Engineering and Physical Sciences, University of Southampton, Southampton, UK

⁴Daido Metal Co. Ltd, European Technical Centre (UK), Ilminster, UK

Correspondence

Songsong Lu, Institute of Solid Mechanics, School of Aeronautic Science and Engineering, Beihang University (BUAA), 37 Xueyuan Road, Haidian District, Beijing 100191, China.
Email: song_lu@buaa.edu.cn

Funding information

Engineering and Physical Sciences Research Council, Grant/Award Number: EP/M50662X/1; Daido Metal Co. Ltd

Abstract

A multilayer overlay coating system containing an intermediate intermetallic layer is an architecture expected to show good fatigue resistance. Experimental characterization and modeling simulations were carried out to classify the different crack initiation mechanisms occurring during fatigue of this coating system (2IML coating system) and to reveal how changes in the layer architecture lead to fatigue improvement. Surface crack initiation seems to play the dominated role in the fatigue failure of this coating system as over 55% of observed cracks were surface cracks. Fatigue improvement is achieved by increasing surface initiation resistance via decreasing the IML-Top layer thickness. However, subsurface initiation mechanisms inhibit the improvement (dominated by surface initiation mechanism) achieved by locating the IML-Top layer closer to the top surface. Optimizing the design of 2IML multilayer coatings based on the fatigue performance should eliminate the unreacted nickel layer in the intermediate IML-Top layer, increase the subsurface interface strength, and decrease the density of voids occurring in the annealing process.

KEYWORDS

characterization, fatigue failure mechanism, finite element analysis, multilayer coatings

1 | INTRODUCTION

The use of multilayer architectures in a thin overlay coating can improve the performance of components against the higher demands proposed in the design of many engineering applications, for example, the lower weight but higher engine output required for engines.^{1,2} In the design of multilayer coatings, hard and soft materials are usually used together as they can provide great improvements in a series of properties, including fatigue

performance, corrosion resistance, conformability, and embeddability.^{1,3–5}

A Sn–Ni multilayer coating system (see Figure 1A) comprising alternating tin–copper and tin–nickel intermetallic (IML) sublayers, denoted in our work as a 2IML multilayer coating system, is such a thin multilayer coating. Considerable improvements in the fatigue resistance have been achieved in this configuration compared with counterparts without the intermediate tin–nickel IML coating layer, denoted in our work as a

This is an open access article under the terms of the Creative Commons Attribution License, which permits use, distribution and reproduction in any medium, provided the original work is properly cited.

© 2022 The Authors. *Fatigue & Fracture of Engineering Materials & Structures* published by John Wiley & Sons Ltd.

IIML multilayer coating (Figure 1B).^{7,9,10} Further experimental investigations indicated that the fatigue performance of this 2IML multilayer coating system can be further improved when decreasing the distance between the middle IML sublayer and the top surface but by decreasing this central IML sublayer thickness.^{6,11} However, the design/optimizing design of this multilayer coatings and such thin multilayer overlay coating architectures with better performance may only be achieved empirically through trial and error. It is because mechanistic understanding of fatigue failure and what controls the improved performance (particularly the fatigue performance) are limited.

Fatigue failure mechanisms in multilayer coatings system are complex. The residual stress is well known to be dependent on the coating layers organization and thickness, for example, the TiN hard coating¹² and Cu/W nanomultilayers.¹³ The microstructure and mechanical properties of some layers in these multilayer coatings may change substantially with changing layer thickness across a thickness range, such as the electroplated Ni/Sn multilayered composites,¹⁴ $(\text{Na}_{0.85}\text{K}_{0.15})_{0.5}\text{Bi}_{0.5}\text{TiO}_3$ multilayer thin films produced by spin coating¹⁵ and multiple type of PVD coatings.¹⁶ Multiple crack initiation mechanisms, including surface crack initiation and a series of different subsurface crack initiation mechanisms, may occur in the failure of multilayer coatings. This is indicated in experimental research on composite TiSiN/Ag/TiSiN multilayer coating¹⁷ and PVD coatings.¹⁸ Subsurface crack initiations may occur due to stress concentrations produced by subsurface characteristics, such as the interface roughness of each layer.^{19–21} These potential crack initiation mechanisms may have different impacts on the fatigue performance as the different stress levels experienced at different locations can lead to different

crack initiation properties (affecting $S-N$ curves) for different material/interfaces²² and different expected shielding/antishielding effects for crack propagation.^{8,23,24}

There are some investigations about fatigue improvement mechanisms of layered architectures. Numerical parametric studies on trilayer architectures of Joyce et al.²⁵ indicated the reduction of soft inter-layer thickness enhances the shielding and provides the improved crack propagation resistance. Zhou et al.²⁶ compared the fatigue performance of bilayer and multilayer Ti/TiN coatings (overall thickness is $1\ \mu\text{m}$) deposited on the Ti46Al8Nb alloy substrate by the hollow cathode deposition method. This investigation indicated the better fatigue performance of multilayer Ti/TiN coatings because of retarding fatigue crack growth more significantly. Most of these researches just reported the improved fatigue performance and explained the corresponding mechanisms initially. The majority of reported mechanisms are highly conjectural and focused on explaining the fatigue resistance in layered architectures qualitatively. Systemic researches on what controls the improved fatigue performance in the optimizing design (designing the architectural parameters) are limited. This retards the optimization of the fatigue performance of layered architectures by designing the architectural parameters.

In this research, the mechanisms of fatigue failure in the 2IML multilayer coating system has therefore been investigated further by more detailed experimental characterization coupled with simulation analysis under the bending condition. Material properties of the different layers in this coating system are studied in more depth to understand whether they are affected by differing layer thickness. Different crack initiation

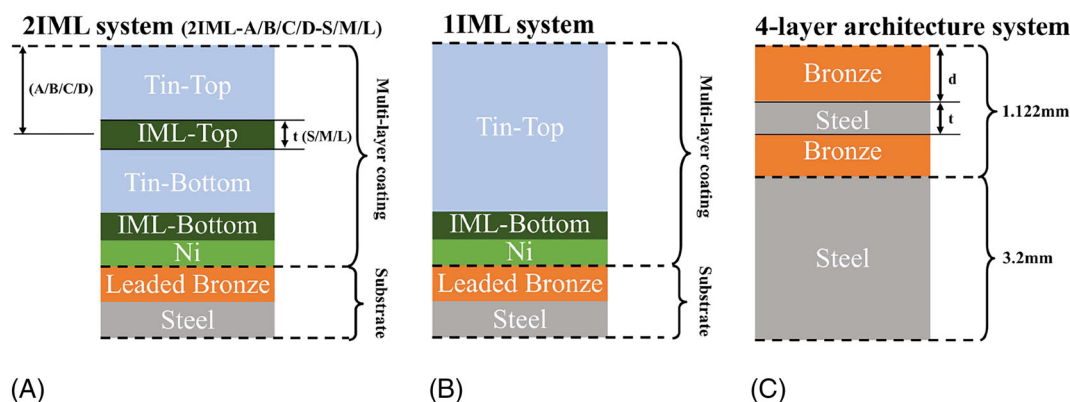


FIGURE 1 Schematic diagram of the cross-sectional architectures of flat samples with (A) 2IML multilayer coatings system,⁶ (B) 1IML coating system,⁷ and (C) four-layer architecture system⁸ [Colour figure can be viewed at wileyonlinelibrary.com]

mechanisms (based on the different initiation locations) and the linked change in the achieved fatigue performance improvement of the 2IML multilayer coating system are analyzed based on posttest observations of coating cross sections and further numerical simulation work. The detailed analysis of these multiple mechanisms will build a basis to optimize the multilayer coating system by controlling the fatigue failure mechanisms via micromechanistically informed architectural design.

2 | MATERIALS AND EXPERIMENTS

2.1 | Samples

2IML multilayer flat samples experimentally investigated in previous research^{6,11} under 3-point bending fatigue tests (see Figure 2A) were studied in further depth in this research by carrying out nanoindentation tests, quantitative posttest observation, and numerical simulation analysis. The samples consist of a 2-mm-thick bilayer substrate and six types of 22- μm -thick multilayer coatings (see Figure 2B). These six multilayer coatings are referred as 2IML-A-M, 2IML-B-S/M/L, 2IML-C-M, and 2IML-D-M coatings, where A/B/C/D represents the location of the IML-Top layer with respect to the top surface of the coatings and S/M/L represents the thickness of the intermediate IML-Top layer increasing from thinner (S) to thicker (L). Their geometries are shown in Figure 2C in detail.

Samples were manufactured by degreasing and etching bilayer substrates first using an alkaline cleaner and a hydrochloric acid solution, respectively. Multilayer coatings were then electroplated layer upon layer in corresponding electrolyte systems, containing Sn^{2+} ions, Cu^{2+} ions, and a proprietary additive package to form tin-based layer and a commercial bath for the nickel-based layer. A thermal annealing procedure was then conducted on all samples at the same temperature and duration time to form the IMLs except for the 2IML-B-L coatings. As a thicker IML-Top layer needs to form by diffusion in the 2IML-B-L multilayer coatings, the duration of its annealing procedure is necessarily longer (around two times). However, there also exists a thin (less than 0.1 μm) undiffused nickel layer in the mid plane of the IML-Top layer in 2IML-B-L multilayer coatings. It should be noted that the materials of each coating layer and processing conditions are the same as that reported before⁷ except the electroplating time (adjusted to produce different layer thickness) and the duration of 2IML-B-L coating's

annealing procedure. Only limited manufacturing information is available as these are proprietary to the sponsoring company.

In previous research,^{6,11} fatigue performance of these six types of multilayer samples were experimentally measured under the 3-point-bend constant amplitude fatigue loads with the same load ratio ($R = 0.1$). Maximum fatigue loads were controlled to ensure the same total strain range ϵ_{Total} (0.0023 at the expected maximum strain zone marked in Figure 2A) was experienced by different multilayer coatings. Their previously reported fatigue lives with the same total strain range ϵ_{Total} were shown in Figure 2D. The ranking of their measured fatigue lives can be found as follows: 2IML-B-S > 2IML-D-M \approx 2IML-C-M > 2IML-B-M > 2IML-A-M > 2IML-B-L (see Figure 2D).

2.2 | Nanoindentation tests

Nanoindentation tests were carried out on a sample with 2IML-C-M coating using a MicroMaterials NanoTest Vantage system (MicroMaterials NTX) equipped with a Berkovich indenter at a stabilized chamber temperature of 21°C. The measured surface was metallographic prepared after being sectioned along the Plane TL. It should be noted that each coating layer in multilayer coating was polished together to reduce the effect of surface preparation on hardness measurement of each coating layers in multilayer coatings (ensuring the surface preparation effects are the same for each coating layers). The hardness and modulus were measured on this surface across a 40 * 33-point matrix in the multilayer coatings, as shown in Figure 3. These indentation tests were depth controlled, where the sample was loaded at a rate of 0.5 mN/s until reaching a 50-nm depth after contacting, then dwelled at this load for 30 s and unloaded at a rate of 1 mN/s. During the testing process, the thermal drift was corrected based on a group of postindentation data gathered with a dwell period of 60 s. The load versus displacement data were also recorded, which were then transferred to load depth curves after being corrected to build the basis for calculating mechanical properties. Based on load depth curves of nanoindentation tests, two mechanical properties (the nanohardness [H] and the reduced elastic modulus [E_r]) were calculated by using the procedure outlined by Oliver and Pharr.²⁷ The measured E_r is a balance value between the material properties of indenter and the test material. The corresponding equation is

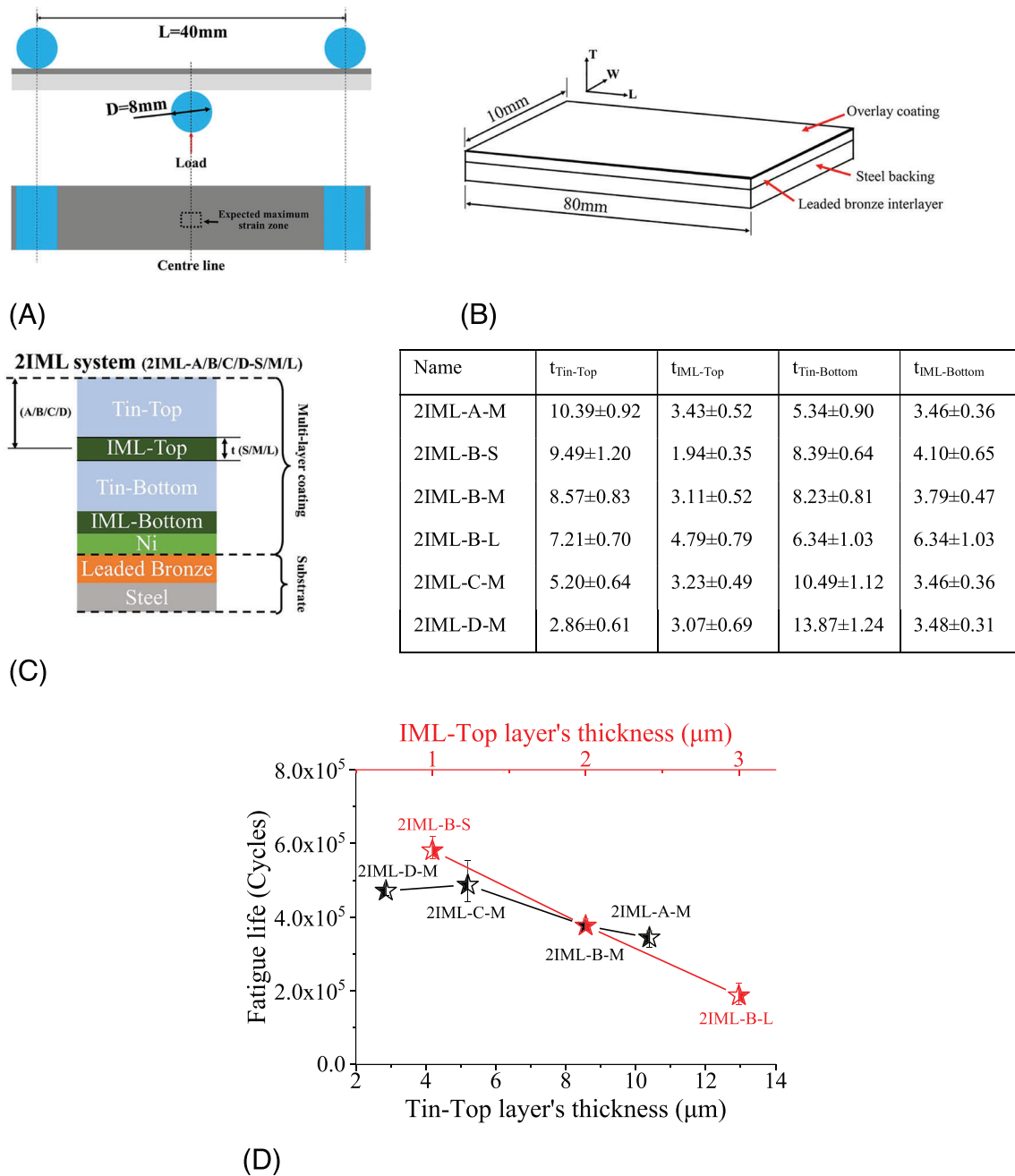


FIGURE 2 (A) Three-point-bend rig, (B) schematic diagram of flat samples with multilayer coatings, (C) cross-sectional structures of 2IML system multilayer coatings (not to scale), where the location of IML-Top layer is away from top surface from A to D and the thickness of IML-Top layer is thicker for M than S, and (D) measured fatigue lives for 2IML multilayer coatings, where the black and red colors are used to mark the effect of IML-Top layer location and thickness, respectively^{6,11} [Colour figure can be viewed at wileyonlinelibrary.com]

$$\frac{1}{E_r} = (1 - \nu_m^2)/E_m + (1 - \nu_i^2)/E_i, \quad (1)$$

where the subscripts m and i refer to the indented material and indenter, respectively. The E_i and ν_i are equal to 1140 GPa and 0.07 for the Berkovich indenter used in this test, respectively.

2.3 | SEM observation of crack path along the thickness direction

The samples listed in Figure 2C and tested under same fatigue conditions (0.002303 total strain range in the expected maximum strain zone and $R = 0.1$) as reported

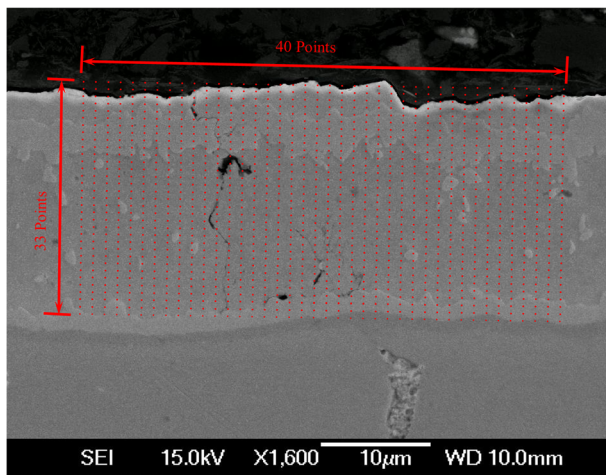


FIGURE 3 Location of a measured 40×33 matrix by nanoindentation [Colour figure can be viewed at [wileyonlinelibrary.com](https://onlinelibrary.wiley.com/doi/10.1111/ffe.13649)]

in previous research^{6,11} were sectioned along the TL plane (the coordinate system marked in Figure 2B). In order to assess the majority of the surface cracks, the length of the sectioned surface along the L direction is comparable to the width of the sample and longer than the diameter of the loading rollers ($D = 8$ mm) shown in Figure 2A.

For all types of 2IML multilayer coatings, representative samples were sectioned. Two samples were sectioned for the 2IML-A-M coatings (denoted as 2IML-A-M-1 and 2IML-A-M-1) while one sample was sectioned for the other coating types. All sectioned surfaces were mounted, ground on successively finer grades of silicon-carbide paper (220, 800, and 1200), and then polished with diamond suspensions (9, 3, and 1 μm) and a colloidal silica suspension (0.06 μm). After these metallographic sample preparation procedures, scanning electron microscope (SEM) was used to observe the cross section and capture all existing crack paths in coatings. It should be noted that over 100 cracks were captured for each sample to allow sufficient statistical analysis.

Quantitative analysis was carried out based on the SEM images using ImageJ 1.52a for each variant of the 2IML multilayer coatings. A series of parameters were measured for the following different cases.

1. The number of surface and subsurface cracks was counted, respectively, to understand the balance between different crack initiation mechanisms (surface/subsurface) with the change of coating architectural parameters.
2. Characteristics of surface cracks marked in Figure 4 were measured in the Tin-Top layer, including the

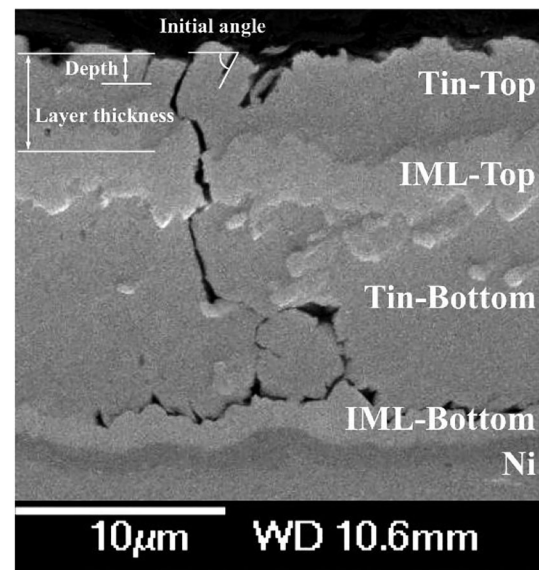


FIGURE 4 Measured values about Tin-Top layer

initial angle, the depth of surface cracks located only in the Tin-Top layer, and the local thickness of the Tin-Top layer at the surface cracks (aiming to normalize with respect to the depth). The distribution values of these parameters were assessed in order to reveal the characteristics of surface initiated cracks.

2.4 | FE model

Stress distribution in the various 2IML multilayer coatings (by varying the location or thickness of IML-Top layer) without cracking were investigated further by numerical simulation work using Abaqus 6.14 based on a 2D FE model. Figure 5 shows the assembly of this model, which consists of a 2D deformable flat strip and a central roller modeled as a discrete rigid body. This 2D deformable flat strip is composed of a multilayer coating with a total thickness of 22 μm and a thicker layer (38 μm) serving as the substrate to provide the appropriate constraint to the modeled coatings. Because the aim of this simulation is to model the stress distribution in multilayer coatings without cracking, interfaces in this 2D deformable flat strip were simply distinguished by defining different material properties on different layers around the interface. This 2D deformable flat strip contacts with the central roller at the intermediate location of its bottom surface with the interaction property of “hard contact” and “rough friction.” Considering the bending load transferred from the substrate to the coatings in the previously reported 3-point-bend experimental research,^{6,11} the flat

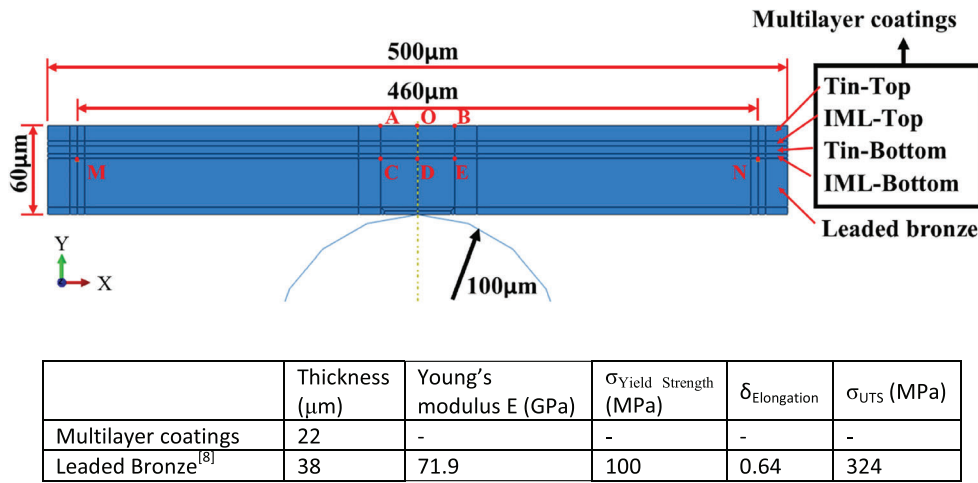


FIGURE 5 FE model of part of leaded bronze substrate and multilayer coatings under 3-point bending condition. Note: Material properties of lead bronze were measured before,¹⁰ and the material properties of each layer in the multilayer coatings (total thickness of multilayer coating is around 22 μm) are measured in this research by nanoindentation tests (listed in Table 3) [Colour figure can be viewed at wileyonlinelibrary.com]

TABLE 1 List of each layer thickness in the different 2IML multilayer coatings in FE models shown in Figure 5

Type	Layer thickness Tin-Top (μm)							
	Tin-Top		IML-Top Tin-Top		Tin-Bottom		IML-Bottom	
	Measured	Modeled	Measured	Modeled	Measured	Modeled	Measured	Modeled
2IML-A-M	10.39 ± 0.92	10.4	3.43 ± 0.52	3.4	5.34 ± 0.90	5.2	3.46 ± 0.36	3.0
2IML-B-S	9.49 ± 1.20	9.5	1.94 ± 0.35	1.9	8.39 ± 0.64	7.6	4.10 ± 0.65	3.0
2IML-B-M	8.57 ± 0.83	8.6	3.11 ± 0.52	3.1	8.23 ± 0.81	7.3	3.79 ± 0.47	3.0
2IML-B-L	7.21 ± 0.70	7.2	4.79 ± 0.79	4.8	6.34 ± 1.03	6.3	6.34 ± 1.03	3.0
2IML-C-M	5.20 ± 0.64	5.2	3.23 ± 0.49	3.2	10.49 ± 1.12	10.6	3.46 ± 0.36	3.0
2IML-D-M	2.86 ± 0.61	2.9	3.07 ± 0.69	3.0	13.87 ± 1.24	13.1	3.48 ± 0.31	3.0

strip in the FE analysis was loaded under 3-point bending conditions applied on the substrate layer. The detailed loading condition was shown in Figure 5, where all movements of two points (Point M and Point N) located on the top surface of substrate with the distance of 460 μm were constrained and the external load was applied via the central roller.

Based on the configurations of samples shown in Figure 2B, FE models consisting of the Tin-Top, IML-Top, Tin-Bottom, and IML-Bottom layers on a leaded bronze layer substrate were established. Six variants were designed based on the following simplification (where the location and thickness of the IML-Top layer were varied to reveal the role of IML-Top layer on the stress distribution):

1. The Ni layer considered as the part of IML-Bottom layer and the total thickness of these two layers was taken to be 3 μm.
2. The overall thickness of multilayer coatings is kept as 22 μm whatever its architecture (achieved by adjusting the thickness of Tin-Bottom layer).

The geometry of these six FE models simplified from various 2IML multilayer coating dimensions are listed in Table 1 in detail. The 2IML-A/B/C/D-M multilayer coatings were designed to study the effect of IML-Top layer's location, where the location of IML-Top layer is represented by the thickness of Tin-Top layer ($t_{Tin-Top}$). The 2IML-B-S/M/L multilayer coatings were designed to study the effect of IML-Top layer's thickness without varying their location (the mid plane). It should be noted that no attempt was made to simulate the effect of interface adhesive strength in this study. The effect of interface adhesive strength has been investigated in our other research and will be reported in other paper.

The flat strip in the FE models was meshed by a structure meshing technique with the maximum mesh size of 1 μm. Mesh in areas contacting the central roller and multilayer coatings were refined with the minimum size of 0.1 μm. Each layer in the multilayer coatings was also meshed by a structure meshing technique. Their mesh size is from 0.1 to 0.5 μm. All elements in this model are four-node reduced integration bilinear plane strain quadrilateral elements (CPE4R). The stress-strain

response of each material in the multilayer coatings was determined by measured mechanical properties in the nanoindentation tests reported here in Section 3 and that of the leaded bronze was described based on mechanical properties measured in previous tensile tests (listed in Figure 5).¹⁰ As only the elastic data can be measured in nanoindentation tests, a linear elastic constitutive model was used for all materials in this simulation work. It should be noted that values of Poisson ratio (ν) for all materials in these FE models were assumed to be 0.33 in the absence of measured data.

In previous experiments (3-point bending fatigue tests), all the 2IML multilayer coatings were tested under the same applied cyclic strain ranges. This was achieved by controlling the applied load only based on the response of bilayer substrate (making the top surface of substrate experience the same total strain range) as the ~22- μm overlay layers will be dominated by the elastoplastic response of 2-mm bilayer substrate.^{6,11} The same method was used to load FE models in this modeling work. The FE models were loaded by controlling the displacements (d_c) in the Y direction of the central roller; see Figure 5. Different d_c values were applied to the FE models with different 2IML multilayer coating architectures to model the conditions of the fatigue experiments (different coatings are compared in terms of the same applied strain level from the bronze interlayer substrate). These different d_c values are to ensure the same strain is

experienced by the different 2IML multilayer coatings along the X direction (represented by the strain ϵ_D at the location of Point D marked in Figure 5). The value of ϵ_D in this simulation work is selected as 0.0025, which is the maximum strain experienced by coatings at the expected maximum strain zone (marked in Figure 2A) in previous fatigue tests.^{6,11} Values of these applied d_c in the FE models with different multilayer coating architectures are listed in Table 2. They were determined by modeling d_c versus ϵ_D curves (calculating the ϵ_D at a series of increased d_c) to find the value of d_c corresponding to the $\epsilon_D = 0.0025$.

3 | RESULTS AND DISCUSSION

3.1 | Mechanical properties of each layer in multilayer coatings

Hardness and reduced modulus for all indented locations were calculated based on load depth curves for the area of a 40 * 33-point matrix shown in Figure 3. The cloud maps of measured nanohardness and reduced modulus are shown in Figure 6A,B, respectively. Compared with Figure 3, these cloud maps can be divided into five rectangular areas based on the location of coating layers (marked by red rectangles in Figure 6A). These areas are identified as Near mounted, Tin-Top, IML-Top related, Tin-Bottom, IML-Bottom related,

TABLE 2 List of applied displacement on the center roller to ensure the same strain levels located at Point D

Strain at the Point D	Displacements of the center roller in the thickness direction (μm)					
	2IML-A-M	2IML-B-M	2IML-CM	2IML-D-M	2IML-B-S	2IML-B-L
0.0025	7.10	7.00	7.16	7.11	6.37	8.00

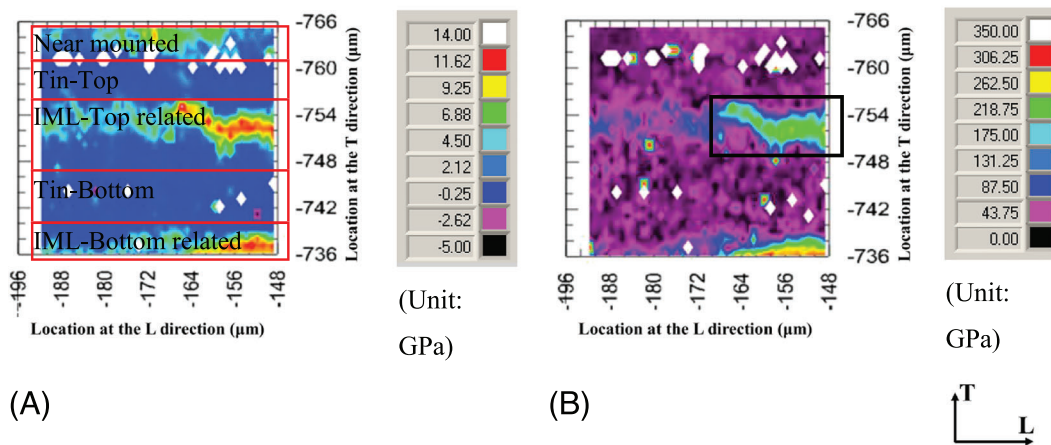


FIGURE 6 Cloud maps of (A) Vickers hardness and (B) reduced modulus in the 2IML-D-M coating [Colour figure can be viewed at wileyonlinelibrary.com]

Tin-Bottom, and IML-Bottom related going from top to bottom.

It can be seen in Figure 6 that the values (represented by color) in areas related to the tin layers (Tin-Top area and Tin-Bottom area) are relatively stable while those in areas related to IML-Top layer locations show significant differences. This indicates the relative stability and instability of measured nanohardness results in the areas of tin-based layers and around IML layers. There are two reasons for this instability in measurement: (1) the thinness of the IML layers along the T direction limits the number of indenters that can be completely located in it and (2) tortuous 3D shape of the IML layers also means that those indenters near the boundary of IML layers are measuring combined properties between IML and tin alloy as the subsurface material below the apparent IML may be the soft tin-based alloy. Therefore, only those data located in a local area with a higher stable nanohardness or reduced modulus value (marked by black rectangle in Figure 6B) can be considered to represent the properties of the IML.

Measured hardness and reduced modulus of both Tin-Top and Tin-Bottom areas are shown in Figure 7A,B. It can be seen that the distribution of measured material properties for Tin-Top and Tin-Bottom areas are similar. This indicates the thickness-independent material properties of the tin-based layers in the studied thickness range (2.86–13.87 μm), where the hardness and reduced modulus are roughly equal to 0.18 and 25 GPa, respectively. Measured material properties of the IML-Top-related area are shown in Figure 7C,D. It should be noted that these measured data represent material properties of the tin layer, IML layer, and different combined degrees of the two as this rectangle contains not only the IML layer but also part of the tin-based layers. The range of material properties for the tin-based alloy (determined in Figure 7A,B) was marked by a gray box in Figure 7C,D. Apart from those data in this marked area, other data measured from the IML-Top-related area are distributed over a wide range, 0.5–15 GPa for hardness, and 50–200 GPa for reduced modulus. The upper limit of this wide range is consistently about 12 and 200 GPa for the hardness and reduced modulus, respectively. These upper limits can also be shown in Figure 7E, where the reduced modulus tends to be stable at this upper level (200 GPa) with an increase of hardness for the IML-Top-related area. Taken together, it seems these upper limits of the hardness and reduced modulus can be construed as the measured material properties of the hardest material (the IML).

All measured reduced moduli for materials in the 2IML multilayer coatings were converted to Young's modulus by using Equation 1, where the Poisson ratio for

all materials are assumed as 0.33, and listed in Table 3 with the measured hardness. The hardness and Young's modulus for tin shown in Table 3 can be applied to tin layers within the thickness range between 2.86 and 13.87 μm because their thickness-independent characteristics are shown in this nanoindentation tests. The strength of tin within this thickness range can also be seen as thickness independence as it is direct related to the hardness.^{28,29} These information of material properties (material data and thickness independence characteristics) will be used in the simulation analyzes discussed in this research to further understand the fatigue failure mechanisms of 2IML multilayer coatings in terms of continuum mechanics.

3.2 | Surface/subsurface crack initiation mechanisms

Both surface and subsurface cracks were found in the SEM cross-sectional observations (as reported previously in detail^{6,11}). A typical observed surface crack can be seen in Figure 10A. It initiates at the top surface of the multilayer coatings due to the local stress concentration linked to the spikiness characteristics of the top surface profile¹¹ and is considered a surface initiation mechanism. The initial angle for all surface cracks and the depth of surface cracks which were only located in the Tin-Top layer (as marked in Figure 4) were assessed for each studied 2IML multilayer coatings except the 2IML-D-M (its thinnest Tin-Top layer produced difficulty in measuring these values) and are shown in Figure 8.

The distribution of initial surface crack angles can be seen in Figure 8A, where two peaks are located at similar locations for different multilayer coatings. The values of these two peaks are 55° and 125°, respectively, and symmetrical about the sample center line, revealing the tendency of crack initiation angle. As intergranular crack growth is generally observed in the tin layer,⁶ this tendency may be due to the available grain boundary orientations of the tin in the Tin-Top layer.

The distribution of surface crack depths is shown in Figure 8B, where the value of depth was normalized with respect to the local thickness of the Tin-Top layer. The percentage of surface cracks propagating through to the bottom surface of the Tin-Top layer were found to be very low in each type of 2IML multilayer coatings (lower than 20%), reflecting the high crack resistance related to the shielding effects when the crack propagates from softer material to harder material.

The percentage of surface cracks in various 2IML multilayer coatings with different IML-Top layer location and thicknesses has been counted in our previous

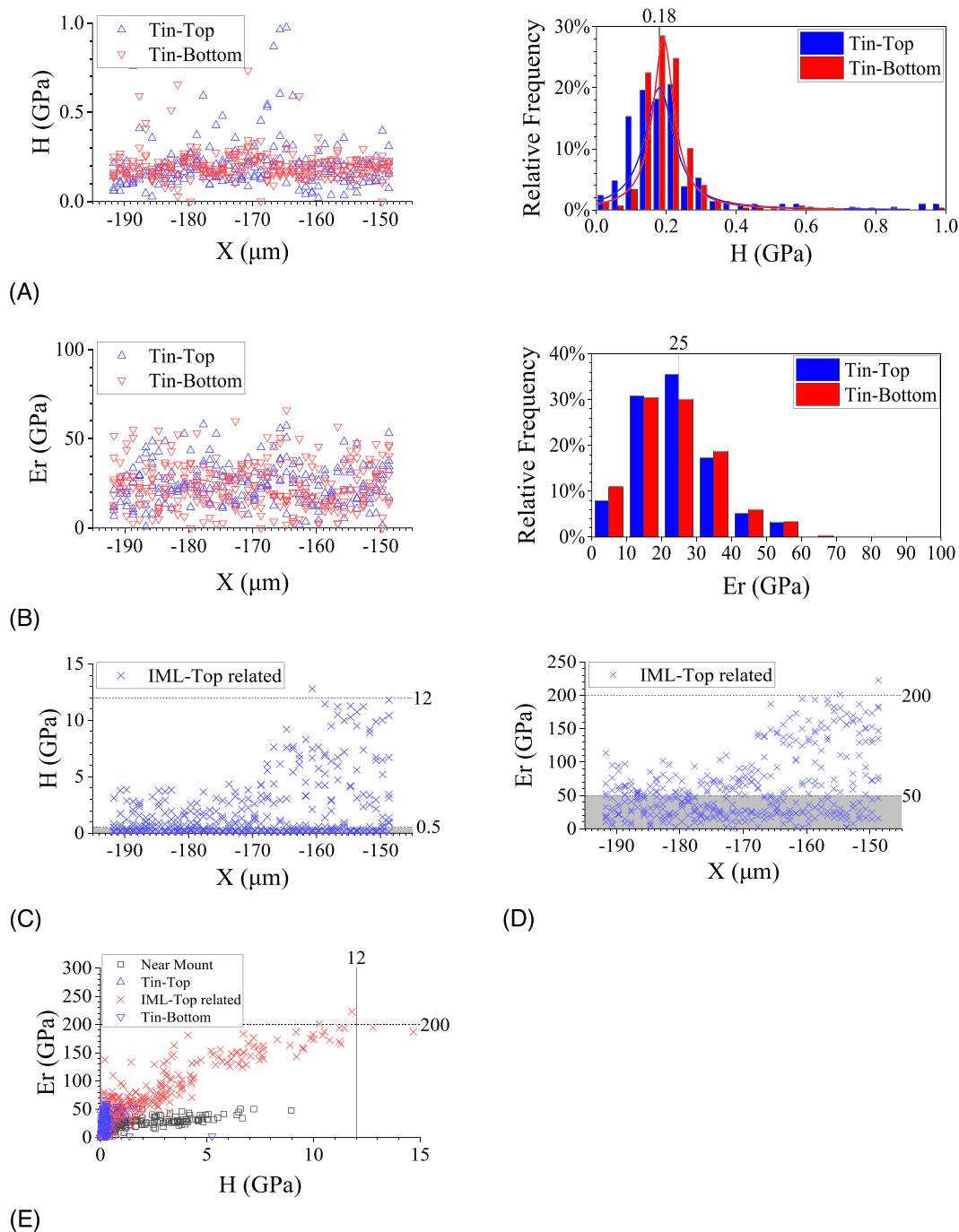


FIGURE 7 (A) Hardness data located in Tin-Top layer and Tin-Bottom layer and corresponding probability distribution, (B) reduced modulus data located in Tin-Top layer and Tin-Bottom layer and corresponding probability distribution, (C) hardness data located in areas around IML-Top layer and IML-Bottom layer, (D) reduced modulus data located in areas around IML-Top layer and IML-Bottom layer, and (E) relationship between hardness and reduced modulus for all nanoindentation data [Colour figure can be viewed at wileyonlinelibrary.com]

TABLE 3 Measured material properties of materials in 2IML multilayer coatings by nanoindentation

	Tin-based alloy	IML
Hardness (GPa)	0.18	12
Young's modulus (GPa)	22.8	215.9

observations^{6,11} and are shown in Figure 9. The percentage of surface cracks (55% or more) outweighs the percentage of subsurface cracks for all architectures, indicating the surface initiation mechanism plays the dominant role in the fatigue failure of these 2IML multilayer coatings. Considering the effect of IML-Top layer

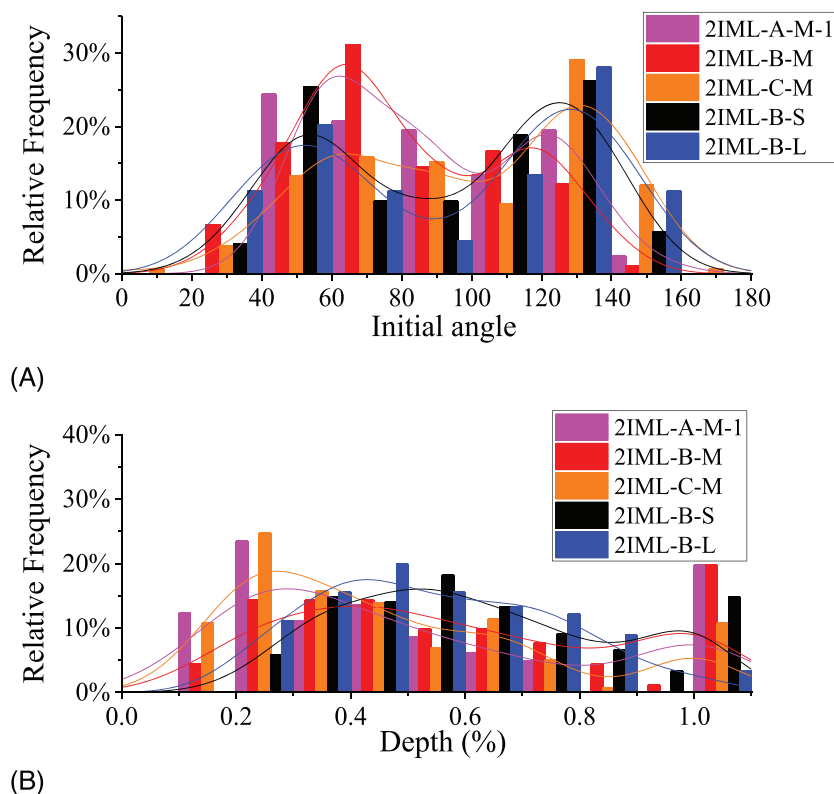


FIGURE 8 Frequency distribution histogram of (A) initial angle of surface cracks and (B) crack depth in Tin-Top layer in studied 2IML multilayer coatings [Colour figure can be viewed at [wileyonlinelibrary.com](https://onlinelibrary.wiley.com/doi/10.1111/ffe.13649)]

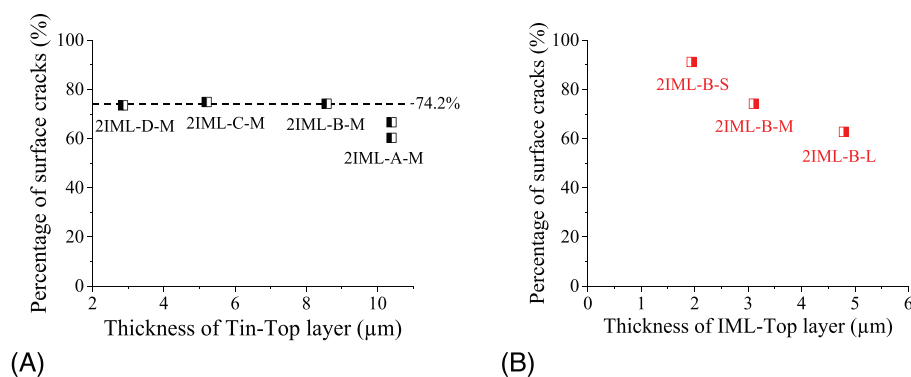


FIGURE 9 Percentage of surface cracks in 2IML multilayer coatings with different (A) location¹¹ and (B) thickness⁶ of IML-Top layer, where A/B/C/D and S/M/L relate to the location and thickness of IML-Top layer shown in Figure 2 [Colour figure can be viewed at [wileyonlinelibrary.com](https://onlinelibrary.wiley.com/doi/10.1111/ffe.13649)]

thickness, the increase of surface crack proportion moving from 2IML-B-L to 2IML-B-S can be seen in Figure 9B. This indicates the increase of surface initiation mechanisms with a decrease of IML-Top layer thickness.

Subsurface cracks related to different subsurface characteristics were captured, indicating the existence of multiple subsurface crack initiation mechanisms. They include subsurface cracks initiated at (1) the remaining unreacted center nickel layer in the intermediate IML-Top layer (see Figure 10B), identified as Ni-induced subsurface initiation mechanism; (2) voids located in tin-based layers (see Figure 10C), identified as void-induced subsurface initiation mechanism; and (3) initiation at subsurface interfaces (see Figure 10D), identified as

interface-induced subsurface initiation mechanism. These crack initiation processes are due to the raised local stress concentrations at subsurface microstructural stress concentrating features (voids or the interface roughness profile) and weaker adhesion properties at subsurface interfaces.

Due to the limited total number of experimentally captured subsurface cracks and as the existence of multiple subsurface crack initiation mechanisms will significantly affect the representativeness of any statistical experimental results, the percentage of each subsurface crack initiation mechanism in the various 2IML multilayer coatings were not counted individually. Their changes with the change of coating architecture will be

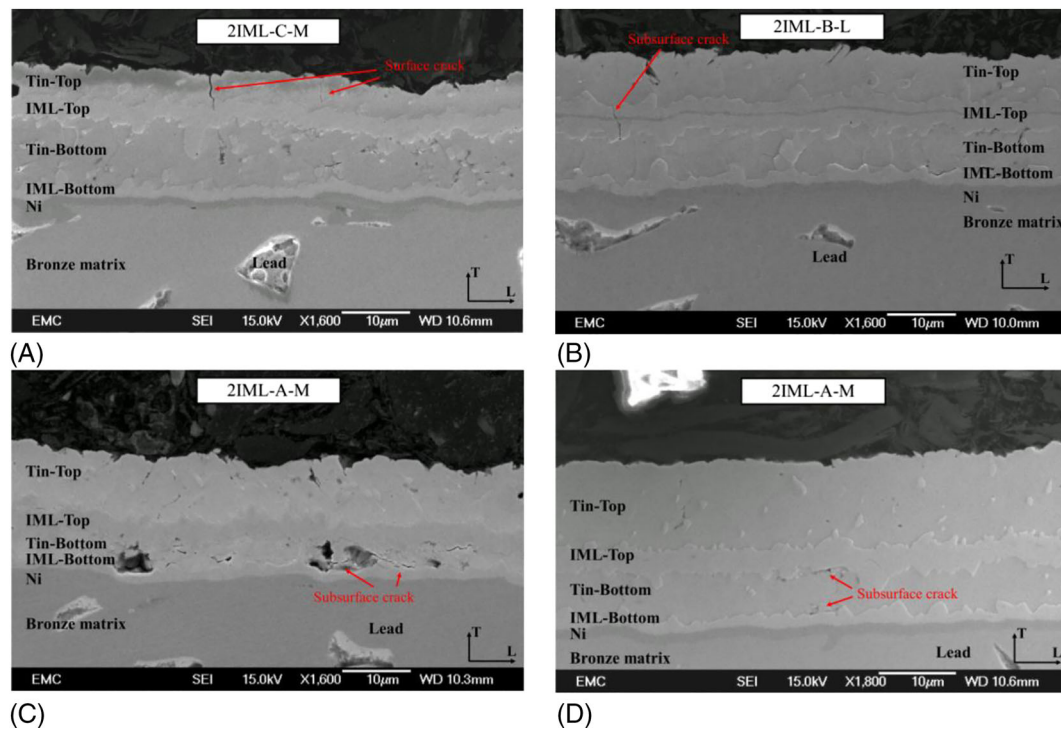


FIGURE 10 (A) Surface cracks and subsurface cracks initiated at the (B) IML layer, (C) interfaces between tin layer and IML layer, and (D) voids [Colour figure can be viewed at [wileyonlinelibrary.com](https://onlinelibrary.wiley.com/doi/10.1111/ffe.13649)]

revealed indirectly by theoretical analysis in the next section.

3.3 | Effect of surface crack initiation mechanism on fatigue life improvement

In the determination of the crack initiation life, fatigue strength and local stress distribution are key factors. The nanoindentation research in Section 3.1 has indicated the thickness-independent characteristics of tin material properties whatever the layer thickness (in the studied thickness range). In line with the mechanical properties of the tin layer,²⁸ the fatigue strength of the Tin-Top layer in various 2IML multilayer coatings (studied in this research) is expected to be similar. As a result, the change of surface local stress distribution in various 2IML multilayer coating architectures (IML-Top layer location and thickness) is expected to correspond to a change of crack initiation life. It should be noted that the local stress distribution is determined by surface roughness and surface stress distribution. As the similar surface roughness of various 2IML multilayer coating architectures studied in this research has been reported in previous research,^{6,11} the change of surface stress distribution is expected to correspond to a change of crack initiation life in terms of

promoting/demoting a surface crack initiation mechanism.

Figure 11A,B shows the stress distribution along the top surface (Line AB in Figure 5) in 2IML multilayer coatings when varying the individual effect of IML-Top layer location (2IML-A/B/C/D-M) and thickness (2IML-B-S/M/L), respectively, where the location of loading line is marked by the dashed line. In each multilayer coating architecture, the simulated variation of von Mises stress on the top surface at the point located at the loading line (Point O in Figure 5) experiences the maximum stress. This indicates that the possibility of surface crack initiation decreases from Point O in both directions (along the Line AB) away from this point. Comparing the surface stress distribution in different 2IML multilayer coatings, the decrease of stress level from the 2IML-A-M to 2IML-D-M in Figure 11A and from the 2IML-B-L to 2IML-B-S in Figure 11B can be found. This decrease of stress level at top surface (Line AB) with the change of IML-Top layer is due to the decrease of stiffness under the loading conditions. Given the similar top surface roughness of all 2IML multilayer coatings,^{6,11} this decrease of stress level represents an expected increase of crack initiation life if the surface crack initiation mechanism predominates. This indicates that an enhancement of surface crack initiation resistance can be achieved by locating the IML-Top

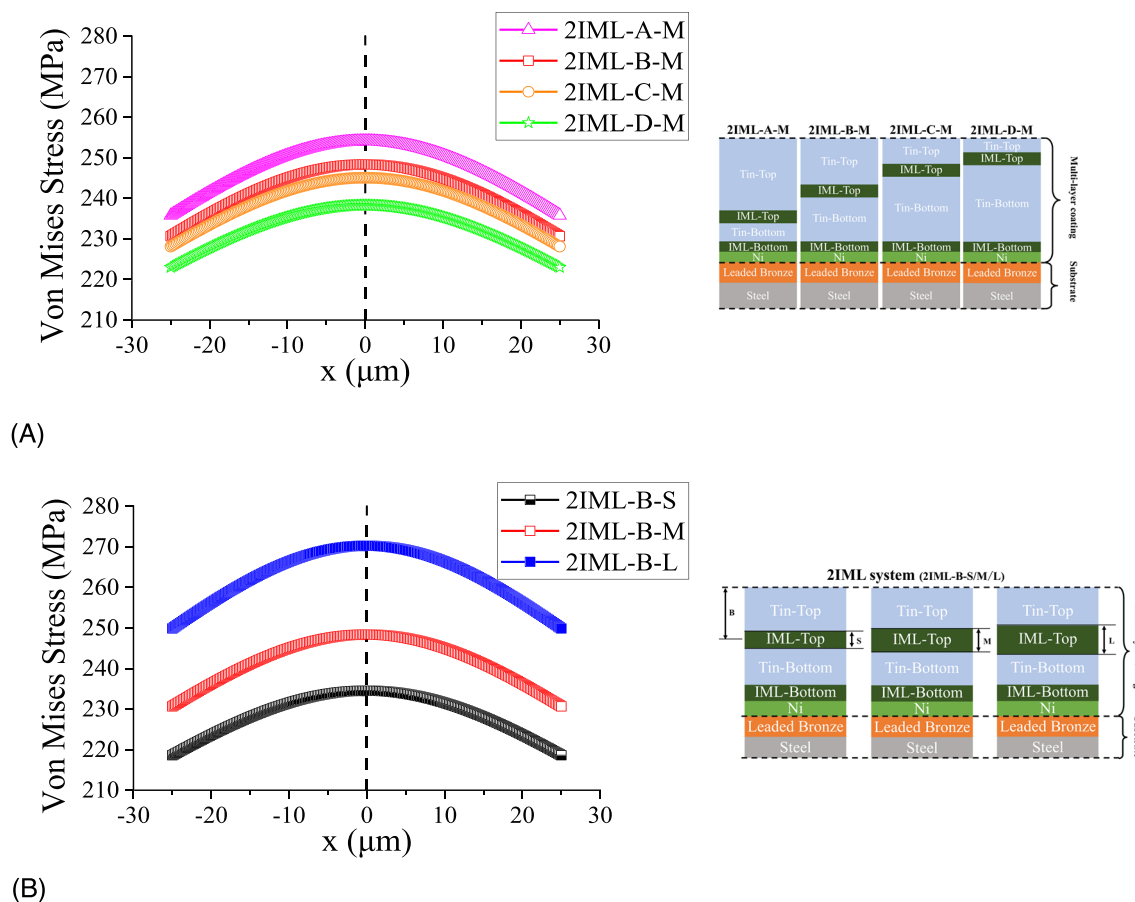


FIGURE 11 von Mises stress distribution along the top surface of overlayer coatings in 2IML multilayer coatings with the different: (A) location of IML-Top layer and (B) thickness of IML-Top layer [Colour figure can be viewed at [wileyonlinelibrary.com](https://onlinelibrary.wiley.com/doi/10.1111/ffe.13649)]

layer closer to the top surface or decreasing the thickness of the IML-Top layer. As the increase of overall fatigue life with these variations of IML-Top layer location and thickness was observed (indicated by previous experimental investigations^{6,11}), reducing the surface initiation mechanism is therefore an important factor controlling the fatigue improvement of 2IML multilayer coatings. The degree of fatigue improvement will be determined after comparing it with what controls other crack initiation mechanisms.

3.4 | Mechanics analysis of subsurface crack initiation mechanisms

Subsurface crack initiation mechanisms in 2IML multilayer coatings investigated in this research have been classified into Ni-induced, void-induced, and interface-induced subsurface initiation mechanism based on different initiation subsurface characteristics (stated in Section 3.2). Investigating the stress distribution along the thickness direction in various 2IML multilayer

coatings can help to understand the effect of coating architectural parameters on subsurface crack initiation mechanisms. The stress distribution along the thickness direction (Line OD/loading line in Figure 5) in 2IML multilayer coatings considering the individual effect of IML-Top layer location (2IML-A/B/C/D-M) and thickness (2IML-B-S/M/L), respectively, are shown in Figure 12A,B, where y represents the depth direction.

In terms of a specific 2IML multilayer coating, the increase of von Mises stress in the same material (whatever the layer they are located in) at the lowest values of y (i.e., closer to the top surface) can be seen. Take the 2IML-B-M multilayer coatings as an example (see Figure 12A), the von Mises stress in the tin increases from 112 MPa at the bottom surface of Tin-Bottom layer ($y = 19.0$) to 234 MPa at the top surface of Tin-Top layer ($y = 0$) and that in IML increases from 746 MPa ($y = 22.0$) at the bottom surface of IML-Bottom layer to 1643 MPa at the top surface of this layer ($y = 8.6$). This stress distribution indicates that the maximum stress in tin and IML is located in the top surface of the Tin-Top layer and IML-Top layer, respectively, thus representing

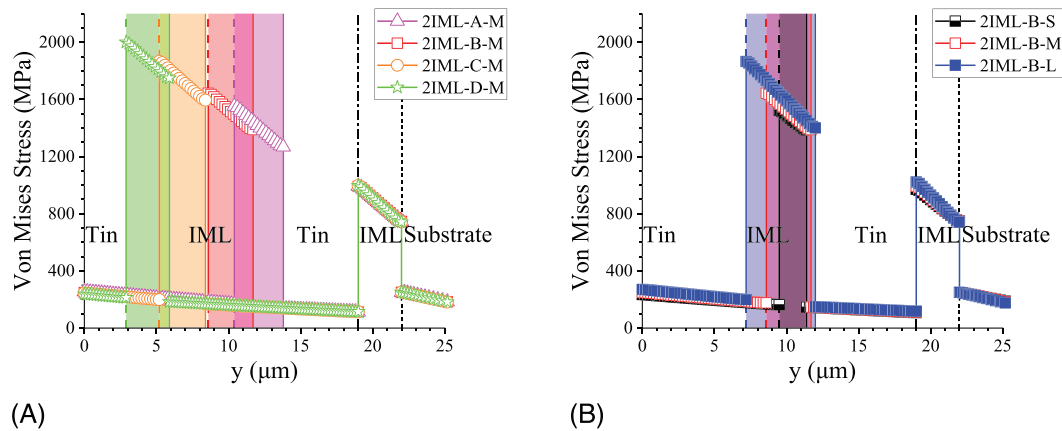


FIGURE 12 von Mises stress distribution along the thickness direction of overlayer coatings in 2IML multilayer coatings with the different: (A) location and (B) thickness of IML-Top layer [Colour figure can be viewed at wileyonlinelibrary.com]

a higher possibility of crack initiation at these two locations (corresponding to a surface initiation mechanism and an interface-induced subsurface initiation mechanism). It should be noted that the considerably higher maximum stress in the IML compared to that in tin does not necessarily represent a higher possibility of an interface-induced subsurface initiation mechanism. This is because there are two other factors that need to be considered in the priority determination of surface and subsurface crack initiation: (a) the stress concentration related to the roughness profile of different interfaces and (b) the fatigue strength for different materials.

Comparing the simulated stress distribution along the thickness direction for different 2IML multilayer coatings, the stress at the same location (the same y value in Figure 12) in the same layer decreases from the 2IML-A-M to 2IML-D-M (see Figure 12A). At the top surface center of 2IML multilayer coatings ($y = 0$ in Tin-Top layer), this decrease of stress is from 254 to 238 MPa. It should be noted that (a) the expected similar fatigue strength of the Tin-Top layer in various 2IML multilayer coatings studied in this research has been stated in Section 3.3 and (b) previous experimental research indicated the tiny effect of IML-Top layer's location on the top surface roughness.¹¹ As a result, this decrease of stress represents the potential increase of crack initiation life under the surface initiation mechanism. This reveals the improvement of crack initiation life if the surface initiation mechanism predominates as more constraint is provided by locating the stiffer IML-Top layer closer to the top surface of 2IML multilayer coatings (corresponding to that revealed in Section 3.3).

However, this higher constraint means more stress is supported by the stiffer IML-Top layer (see Figure 12A). Thickness-independent mechanical properties of IML in the studied thickness range have been indicated in Chen

et al.³⁰ In line with its mechanical properties,²⁸ the fatigue strength of IML layer in various 2IML multilayer coatings (studied in this research) is expected to be similar in various 2IML multilayer coatings studied in this research. In terms of top/bottom interfaces of IML-Top layer in various 2IML multilayer coatings studied in this research, the fatigue strength can also be expected to be similar. The reasons are their similar roughness parameters and manufacturing process. Therefore, more stress supported by the stiffer IML-Top layer represents potentially easier subsurface crack initiation related to the IML-Top layer (also shorter crack initiation life under the interface-induced subsurface initiation mechanism and Ni-induced subsurface initiation mechanism for similar roughness interfaces¹¹). They are opposite to that predicted if surface initiation mechanism occurs. This indicates that the effect of locating the IML-Top layer closer to the top surface on the crack initiation life depends on the balance of different crack initiation mechanisms.

The decrease of stress at the same location (same y) in the same layer going from the 2IML-B-L to 2IML-B-S can be seen in Figure 12B. At the top surface center of 2IML multilayer coatings ($y = 0$ in Tin-Top layer), the stress decreases from 270 to 234 MPa. This indicates more cycles will be required for crack initiation under the surface initiation mechanism in 2IML multilayer coatings with the thicker IML-Top layer because (a) the similar top surface roughness for 2IML-B-S/M/L have been indicated in previous experimental research⁶ and (b) the similar fatigue strength of Tin-Top layer in the studied thickness range has been stated in Section 3.1. In other words, the effect of decreasing the IML-Top layer thickness on the crack initiation life under the surface initiation mechanism is the same as that of locating the IML-Top layer closer to the overlay coatings' top surface.

However, the decrease of stress in the IML-Top layer with the decrease of the IML-Top layer thickness can be found in Figure 12B (this is opposite to the change of stress level by locating the IML-Top layer closer to the overlay coatings' top surface). This represents a predicted increase of crack initiation life under crack initiation mechanisms related to the IML-Top layer, given the similar interface roughness and fatigue strength of this layer.⁶

In terms of change of void-induced subsurface initiation mechanism in various 2IML multilayer coatings, the fatigue strength, voids distribution, and stress distribution in the Tin-bottom layer need to be considered. The fatigue strength of the Tin-Bottom layer in various 2IML multilayer coatings studied in this research was also expected to be similar due to the thickness independence characteristics of tin mechanical properties. As a result, the distribution of voids and stress in the Tin-Bottom layer are main factors affecting the potential crack initiation life under the void-induced subsurface initiation mechanism. Size-dependent characteristics of voids in Tin-Bottom layer have been indicated in previous experimental research.⁶ They are formed due to the volume change of the thin and constrained Tin-Bottom layer in the formation process of the top and bottom IML layers, where the tin diffuses into the two Ni layers under annealing (diffusion from the surface Sn layer will not form voids as the surface is not constrained).^{7,10,11} For the same IML layer thickness ($\sim 3 \mu\text{m}$), the total volume of these voids is a smaller proportion of a thicker Sn bottom layer because the same volume change is required. As these voids will raise the local stress concentration

and result in crack initiation, a smaller proportion of these voids in the Tin-Bottom layer will result in a decrease possibility of crack initiation under the void-induced initiation mechanism.

By locating the IML-Top layer closer to the top surface without varying the thickness of IML-Top layer (from 2IML-A-M to 2IML-D-M), the thickness of Tin-Bottom layer increases, with a corresponding expected decrease of proportion of voids in the Tin-Bottom layer. Besides, the decrease of stress in Tin-Bottom layer at the same location (same y value) can be seen in Figure 12A. The crack initiation life of the void-induced initiation mechanism is therefore deduced to increase. In terms of the effect of IML-Top layer thickness, decreasing thickness (from 2IML-B-L to 2IML-B-S) will also lead to an increase of Tin-Bottom layer thickness (see Figure 2C). As less volume change of Sn is required to form the thinner IML layer, the total volume of voids is expected to be a smaller proportion of a thicker Sn bottom layer. This will result in the decrease void-induced subsurface initiation mechanism. Besides, the decrease of stress in Tin-Bottom layer at the same location (same y value) can be seen in Figure 12B. The crack initiation life of the void-induced initiation mechanism is therefore deduced to increase. Crack initiation mechanism information revealed by the FE analysis reported here is summarized in Table 4, including the crack initiation location, the stress change at this location, the related change in crack initiation possibility in determining the fatigue resistance improvement of coatings, and the potential change of crack initiation life under corresponding crack initiation

TABLE 4 The changes of stress level, possibility of crack initiation, and potential crack initiation life corresponding to each crack initiation mechanism with the effect of IML-Top layer's location and thickness in the fatigue resistance improvement of 2IML multilayer coatings

Type of crack initiation mechanisms	Fatigue resistance improvement in the 2IML multilayer coatings					
	Locating the IML-Top layer closer to the top surface			Decreasing the thickness of IML-Top layer		
	Stress level	Possibility of crack initiation	Potential crack initiation life	Stress level	Possibility of crack initiation	Potential crack initiation life
Surface initiation mechanism	Decrease	Decrease	Increase	Decrease	Decrease	Increase
Ni-induced subsurface initiation mechanism	Increase	Increase	Decrease	Decrease	Decrease	Increase
Interface-induced subsurface initiation mechanism	Increase	Increase	Decrease	Decrease	Decrease	Increase
Void-induced subsurface initiation mechanism	Decrease	Decrease	Increase	Decrease	Decrease	Increase

Note: The void-induced subsurface initiation mechanism is dominated by stress concentrations associated with voids; therefore, they are not considered in this analysis.

mechanisms. They are summarized in terms of designing coating architectural parameters to improve the fatigue performance (i.e., locating the IML-Top layer closer to the top surface or decreasing the thickness of IML-Top layer). By locating the IML-Top layer closer to the top surface, the reduction of fatigue lifetimes under interface-induced and Ni-induced subsurface initiation mechanism can be found. They are opposite to that predicted if surface initiation mechanism or void-induced subsurface initiation mechanism, indicating that these two subsurface initiation mechanisms may ultimately hinder the improvement of fatigue performance possible in 2IML multilayer coatings. By decreasing the thickness of IML-Top layer, a similar effect (improving the fatigue performance) on the fatigue performance of 2IML multilayer coatings can be found for all initiation mechanisms (surface, Interface-induced subsurface and Ni-induced subsurface). It should be noted that the same effect is seen for all crack initiation mechanisms with varying the thickness of the IML-Top layer but the opposite effect is seen with varying the location of IML-Top layer on fatigue performance. Thus, the simulation indicates that varying the thickness of IML-Top layer will improve the fatigue performance of 2IML multilayer coatings more significantly than varying the layer location. This also corresponds to the results reported in our previous fatigue tests,^{6,11} where the measured fatigue life of 2IML multilayer coatings with the thinnest IML-Top layer (2IML-B-S) is higher than that of other coatings.

In summary, optimizing the design of 2IML multilayer coatings based on the fatigue performance should aim to further decrease the occurrence of subsurface crack initiation related to the IML-Top layer via improvement of the manufacturing technique. The following manufacturing aims would avoid these subsurface initiation mechanisms: (1) ensure the Ni-Top layer is fully reacted in the annealing process (eliminate the unreacted nickel layer in the intermediate IML-Top layer) to decrease the possibility of crack initiation under Ni-induced subsurface initiation mechanism; (2) increase the subsurface interface strength and decrease its roughness to decrease the possibility of crack initiation under the interface-induced subsurface initiation mechanism; and (3) lower the density of voids occurring in the annealing process to decrease the possibility of crack initiation under void-induced subsurface initiation mechanism.

4 | CONCLUSIONS

Variation in the mechanism of fatigue failure in 2IML multilayer overlayer coatings with coating architectural

parameters was investigated in this research (i.e., locating the IML-Top layer closer to the top surface or decreasing the IML-Top layer thickness). Experimental work was carried out to measure the mechanical properties of each layer and to observe the crack morphologies on the sectioned surfaces of various multilayer coatings. Numerical simulation and theoretical analysis were conducted to understand fatigue failure mechanisms, in particular the change between each crack initiation mechanism. The following conclusions can be drawn:

1. In the thickness range (2.86–13.87 μm), no significant size dependence behavior for the material properties of the tin-based layers was observed. In line with the material properties, the fatigue performance of tin is expected to be similar in this thickness range.
2. In 2IML multilayer coatings, the crack initiates at surface of overlay coatings and a series of subsurface characteristics, including voids, remaining unreacted nickel layer in the IML and interface features.
3. Over 55% of cracks observed were surface cracks in all configurations. Locating the IML-Top layer closer to the top surface or decreasing the thickness of this layer can reduce the stress level at the top surface, representing the enhancement of surface crack initiation resistance. As this trend in expected crack initiation lives agrees with measured fatigue lives in previous fatigue tests (varying IML-Top layer location and thickness), the surface initiation mechanism is clearly an important factor in the fatigue performance improvement of 2IML multilayer coatings.
4. Due to the decrease of stress and void distribution in Tin-Bottom layer, the potential crack initiation possibility under the void-induced subsurface crack initiation mechanism decreases when locating the IML-Top layer closer to the top surface or increasing the thickness of this layer (help to improve the fatigue performance). Due to the change of stress distribution in IML-Top layer and the similar fatigue strength at the same subsurface characteristics, Ni-induced and interface-induced subsurface initiation mechanisms help to achieve fatigue performance improvement of 2IML multilayer coatings by decreasing the IML-Top layer thickness. But they may retard the fatigue performance improvement of 2IML multilayer coatings by moving the IML-Top layer location closer to the top surface.
5. Optimizing the design of 2IML multilayer coatings based on the fatigue performance should eliminate the unreacted nickel layer in the intermediate IML-Top layer (decrease the Ni-induced subsurface initiation possibility), increase the subsurface interface strength and decrease its roughness (decrease the

Interface-induced subsurface initiation possibility), and lower the density of voids occurring in the annealing process (decrease the void-induced subsurface initiation possibility).

ACKNOWLEDGMENTS

This work was supported by the Engineering and Physical Sciences Research Council (EPSRC, EP/M50662X/1) and Daido Metal Co. Ltd.

AUTHOR CONTRIBUTIONS

Songsong Lu: Methodology, investigation, writing – original draft. **Richard Cook:** Investigation, validation. **Yi Zhang:** Project administration, funding acquisition. **Philippa Reed:** Supervision, project administration, funding acquisition, writing – review & editing.

DATA AVAILABILITY STATEMENT

The accompanying data presented in this paper can be found via the doi: <https://doi.org/10.5258/SOTON/D1900>.

ORCID

Songsong Lu  <https://orcid.org/0000-0001-7591-434X>

REFERENCES

- Kopreliovich D Bearing in internal combustion engines; 2018. <http://www.substech.com/> (accessed 30 July 2018).
- Bajpai R, Chandrasekhar U. *Innovative Design and Development Practices in Aerospace and Automotive Engineering*. Springer; 2017.
- Yuan Z, Guo Y, Li C, et al. New multilayered diamond/ β -SiC composite architectures for high-performance hard coating. *Mater Des*. 2020;186:108207
- Pogrebniak A, Beresnev V, Bondar O, et al. Superhard CrN/MoN coatings with multilayer architecture. *Mater Des*. 2018; 153:47-59.
- Finnev J, Evans R. Extending the fatigue life of multi-layer metal joints. *Fatigue Fract Eng Mater Struct*. 1995;18(11):1231-1247.
- Lu S, Cook R, Zhang Y, Reed P. Effect on overall fatigue performance of varying thickness of an intermetallic sublayer within a soft multilayer coating. *Int J Fatigue*. 2021;146:106155
- Zhang Y, Tudela I, Pal M, Kerr I. High strength tin-based overlay for medium and high speed diesel engine bearing tribological applications. *Tribol Int*. 2016;93:687-695.
- Lu S, Laborda A, Cook R, Zhang Y, Verbickas R, Reed P. A numerical study of crack shielding/anti-shielding in layered architectures. *Int J Fatigue*. 2019;124:503-519.
- Laborda A, Robinson A, Wang S, Zhang Y, Reed P. Fatigue assessment of multilayer coatings using lock-in thermography. *Mater Des*. 2018;141:361-373.
- Laborda A, Fatigue of multilayer coatings for plain bearings. Doctoral dissertation. University of Southampton. 2018.
- Lu S, Cook R, Zhang Y, Reed P. Investigating the fatigue performance of soft multilayer coatings with varying locations of an intermetallic interlayer. *Int J Fatigue*. 2020; 145:106130
- Todt J, Zalesak J, Krywka C, Keckes J. Influence of gradient residual stress and tip shape on stress fields inside indented TiN hard coating. *Adv Eng Mater*. 2021;23(11): 2100130
- Romano-Brandt L, Salvati E, Le Bourhis E, et al. Nano-scale residual stress depth profiling in Cu/W nano-multilayers as a function of magnetron sputtering pressure. *Surf Coat Technol*. 2020;381:125142
- Wang W, Singh R. Influence of the microstructure on the mechanical properties of Ni/Sn multilayered composites. *Mater Sci Eng A*. 1999;271(1-2):306-314.
- Wu Y, Or S. Thickness-dependent structural and electromechanical properties of $(\text{Na}_{0.85}\text{K}_{0.15})_{0.5}\text{Bi}_{0.5}\text{TiO}_3$ multilayer thin film-based heterostructures. *Mater Des*. 2018;149: 153-164.
- Gopkalo A, Rutkovskii A. The effect of PVD coatings on the tensile strength and low-cycle fatigue resistance of stainless steel and titanium alloys. *Fatigue Fract Eng Mater Struct*. 2011; 34(12):1012-1020.
- Dang C, Yao Y, Olugbade T, Li J, Wang L. Effect of multi-interfacial structure on fracture resistance of composite TiSiN/Ag/TiSiN multilayer coating. *Thin Solid Films*. 2018;653: 107-112.
- Zha X, Jiang F, Xu X. Investigating the high frequency fatigue failure mechanisms of mono and multilayer PVD coatings by the cyclic impact tests. *Surf Coat Technol*. 2018; 344:689-701.
- Ås S, Skallerud B, Tveiten B. Surface roughness characterization for fatigue life predictions using finite element analysis. *Int J Fatigue*. 2008;30(12):2200-2209.
- Zavattieri P, Hector L, Bower A. Cohesive zone simulations of crack growth along a rough interface between two elastic-plastic solids. *Eng Fract Mech*. 2008;75(15): 4309-4332.
- Okazaki M, Okamoto M, Harada Y. Interfacial fatigue crack propagation in Ni-base superalloy protective coatings. *Fatigue Fract Eng Mater Struct*. 2002;24(12):855-865.
- Suresh S. *Fatigue of Materials*. Cambridge University Press; 1998.
- Sugimura Y, Lim P, Shih C, Suresh S. Fracture normal to a bimaterial interface: effects of plasticity on crack-tip shielding and amplification. *Acta Metall Mater*. 1995;43(3): 1157-1169.
- Suresh S, Sugimura Y, Tschegg E. The growth of a fatigue crack approaching a perpendicularly-oriented bimaterial interface. *Scr Metall Mater*. 1992;27(9):1189-1194.
- Joyce M, Reed P, Syngellakis S. Numerical modelling of crack shielding and deflection in a multi-layered material system. *Mater Sci Eng A*. 2003;342(1-2):11-22.
- Zhou Y, Rao GB, Wang JQ, et al. Influence of Ti/TiN bilayered and multilayered films on the axial fatigue performance of Ti46Al8Nb alloy. *Thin Solid Films*. 2011;519(7): 2207-2212.
- Oliver W, Pharr G. An improved technique for determining hardness and elastic modulus using load and displacement sensing indentation experiments. *J Mater Res*. 1992;7(6):1564-1583.

28. Li Z, Wang Q, Luo A, et al. Fatigue strength dependence on the ultimate tensile strength and hardness in magnesium alloys. *Int J Fatigue*. 2015;80:468-476.
29. Khodabakhshi F, Haghshenas M, Eskandari H, Koohbor B. Hardness–strength relationships in fine and ultra-fine grained metals processed through constrained groove pressing. *Mater Sci Eng a*. 2015;636:331-339.
30. Chen Z, He M, Balakrisnan B, Chum C. Elasticity modulus, hardness and fracture toughness of Ni₃Sn₄ intermetallic thin films. *Mater Sci Eng A*. 2006;423(1-2):107-110.

How to cite this article: Lu S, Cook R, Zhang Y, Reed P. Control of fatigue failure mechanisms in multilayer coatings by varying the architectural parameters of an intermetallic interlayer. *Fatigue Fract Eng Mater Struct*. 2022;45(4):1035-1051. doi:10.1111/ffe.13649